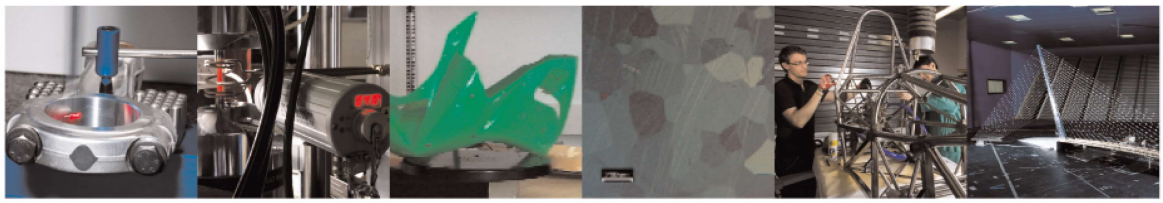

Characterisation of freeform, structured surfaces in T-spline spaces and its applications

Wang, Jian; Zou, Renqi; Colosimo, B M; Lu, Wenlong; Xu, Long; Jiang, Xiangqian (Jane)

This is a post-peer-review, pre-copyedit version of an article published in Surface Topography: Metrology and Properties. The final authenticated version is available online at: http://dx.doi.org/10.1088/2051-672X/abf408

Characterisation of freeform, structured surfaces in T-spline spaces and its applications

Jian Wang[1], Renqi Zou[1], Bianca Maria Colosimo[2], Wenlong Lu[1,*], Liping Zhou [1], and Xiangqian Jane Jiang[3]

[1] State Key Lab of Digital Manufacturing Equipment and Technology, Huazhong University of Science and Technology, Wuhan 430074, China
[2] Politecnico di Milano, Dip. di Meccanica, via G. La Masa 1, 20156 Milano, Italy
[3] EPSRC Centre for Innovative Manufacturing in Advanced Metrology, University of Huddersfield, Huddersfield HD1 3DH, UK
E-mail: hustwenlong@mail.hust.edu.cn

Received xxxxxx
Accepted for publication xxxxxx
Published xxxxxx

Abstract

In advanced manufacturing, surface topographical designs with deterministic freeform and embedded structures have proven to contain effective, additive functionalities. These surfaces need to be geometrically characterised regarding the designed form and structures. However, this is problematic since existing characterisation techniques such as polynomial form removal, Gaussian/spline/wavelet filtration, field-based statistical parameterisation, spectral and fractal analysis do not provide satisfying results. In this paper, we, therefore, propose to characterise the complex surfaces in T-spline spaces, i.e. basis spline spaces along with T-junctions, using an efficient T-spline fitting algorithm. Several case studies show that the proposed method is compatible and has notable potentials for the challenging characterisation tasks, including non-Euclidean freeform removal, edge-reserving filtration with multiscale analysis, scattered data interpolation and smoothing, and smart large-data downsampling or compression.

Keywords: Surface topography, characterisation, T-splines

1. Introduction

Characterisation of engineered surface topography usually comprises areal profiling of a surface portion and its subsequent analyses [1, 2]. A series of techniques and their standards have been developed for the task, e.g. ASME B46.1, ISO 4287 and 25178 series [3-5], to compare results from different users. In these standards, a set of characterising parameters and functions have been developed, such as surface filtration with Gaussian, splines and wavelets; form removal with least square or minimum zone polynomial fitting; height, spatial and hybrid parameters based on field statistics; areal and volume parameters based on material ratio analysis; and analysis with auto-correlation, Fourier transform and fractals [5-8]. Novel watershed segmentation-based feature characterisation techniques [9, 10] further enable particle-like geometrical features of surface topography to be flexibly recognised and analysed. These techniques can characterise general, stochastic features-dominated surfaces with a primitive shape. However, they are reported to produce distorted results [11] when dealing with advanced surfaces, such as those with designed freeform or embedded with micro/nano-structures [12]. These surfaces are usually developed for additive function control, e.g. with improved friction, wear, lubrication, corrosion, hydrophobicity, bio-interactions and optical reflectivity or diffraction [13-18].

1.1. Characterisation challenges

The main characterisation challenges brought by freeform, structured surfaces include the following aspects:

1) Freeform removal.

To evaluate manufacturing errors in varying scales or frequency domains, e.g. waviness and roughness [2], underlying form and form errors must first be removed. For

this purpose, as presented in Figure 1(a), existing techniques such as polynomial fitting is reported to present distortion. This can be attributed to the following two reasons: first, polynomial models with a limited order is not flexible for complex geometric fitting; Second, current fitting methods are planar projection-based, where height deviations of measured points from a fitted model is simply minimised, instead of working with normal distances. Therefore, new non-Euclidean freeform fitting methods with flexible representing models need to be developed [19-21].

2) Filtration and smoothing.

Analysis of surface topography is usually conducted on a specific scale or multiple-scale domain, for which unwanted scale components, like noise and periodic tool marks, need to be smoothed or removed. For this process, mature filtering algorithms have been developed, including the ISO standardised Gaussian, morphological, spline and wavelet filters [6, 22, 23]. However, as presented in Figure 1(b), these methods treat all surface points isotropically, which distorts valid feature edges or boundaries when suppressing the measurement noise. For precision edge-preserving filtration, anisotropic diffusion filters, based on partial differential equations, have recently been developed [19]. However, the existing numerical difference-based algorithms only apply to regular, grid data [24].

3) Interpolation and reconstruction.

Interpolation of grid or scattered sample set for missing data restoration, and reconstruction from a sample set to a mathematical model for reverse engineering, are widely found in engineering surface measurement. They are both required to construct a continuous model either locally or globally. There are many explicit and implicit, parametric and non-parametric methods developed for these purposes, e.g. neighbour averaging, polynomial and spline interpolation, radial basis functions and kriging [25-27]. Among them, B-spline and NURBS have proved to be flexible and robust for freeform reconstruction. However, evidence [28, 29] shows that they are not an optimal solution when reconstructing geometry with complex, sparse features. For example, as presented in Figure 1(d), a laser textured surface topography for hydrodynamic control [30] is reconstructed via NURBS with superfluous control points in each parametric row and column.

4) Down-sampling and compression.

Process control with large-area full-field inspection instead of statistical sampling [31, 32] is highly expected for high-reliability manufacturing. For this purpose, large measurement data of a 3D freeform object from multiple sensors or inspection views need to be fused, compressed and characterised efficiently [33]. Therefore, intelligent algorithms for complex point cloud down-sampling, compression and compatible reconstruction are required [34]. Many smart down-sampling algorithms, e.g. adaptive subdivision and iso-parametric sampling [35], have been developed. A smart down-sampling example from a human face is presented in Figure 1(c) in which dense sample points are located at the features with complex geometries, e.g. eyes, nostrils and lips. However, very few of them have been widely accepted as a default for practical use.

5) Other Challenges

Other challenges include automatic freeform matching and stitching. The former registers a measured freeform point cloud to a CAD model for error evaluation; the latter breaks the range limitation of a sensor by fusing locally measured surface portions to a complete, unified dataset. Due to the geometrical or structural similarities of freeform, structured surfaces, general registration algorithms based on local, statistical feature descriptions, e.g. heat kernel signatures and fast point feature histogram [36], easily result in a high probability of failure. Further challenges may include exact feature extraction, contouring analysis and geometrical morphing [37].

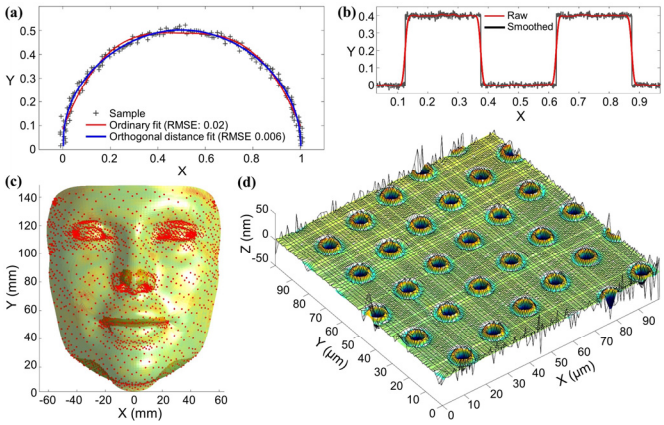

Figure 1. Characterisation challenges of freeform, structured surfaces. (a) Ordinary three-knot uniform NURBS fit produces a remarkable fitting error, compared to an orthogonal distance fit using the same model; (b) noise removal distorts feature edges; (c) 1,000 point smart down-sampling of a dense human face dataset with a root mean squared error of 0.3 mm; (d) NURBS reconstruction of a hard-disk landing zone produces 14,400 control points (black cross vertices) with a peak to valley error of 1 nm.

1.2. Surface characterisation using splines

A spline is a piecewise, polynomial function $f(x)$ that is usually derived with minimised curvature $\int f''(x)^2 dx$. Splines have been extensively used for interpolation, smoothing and modelling-related problems in computer-aided geometrical designs, graphics and digital signal processing [37]. For example, thin-plate splines in the form of global, radial basis functions were used for medical imaging and climate surface interpolation [38, 39]. Cardinal splines [40] were used as a standard to filter regularly spaced data in mechanical engineering [41]. As an important type, B-splines, mainly 4th order B-splines are extensively used in various scientific and engineering problems, including electromagnetic scattering or diffraction, computed

tomography and magnetic resonance imaging, freeform architecture and manufacturing modelling, and manufacturing error analysis [42-46].

Along with the development of wavelet theory and shift-invariant space theory [47-49], B-splines and their rational versions (NURBS) [50] are recognised as probably the best options for signal approximation. A B-spline of degree (r-1) can be defined in the following form:

$$f(u) = \sum_{i=1,\dots,n} c_i \beta_i^r (u - u_i) \quad (1)$$

where $u \in \mathbb{R}$ is a parametric location; $\{u_i\}$ is a sequence of parametric knots of size n, including r repeating (or non-repeating) knots at the borders; c_i is the coefficients or control points of the spline model; while β_i^r is a basis function of order r associated to the i^{th} knot, which can be conveniently calculated using de Boors' recursion formula [51]. Assuming that knots are equidistant, e.g. integers, the basis functions of different orders are presented in Figure 2(a). Eq. (1) also applies to two-dimensional (2D) cases by using tensor product basis functions $\beta(\cdot)$ in the parametric space of $\mathbb{R}^2$. B-splines have the following advantages.

1) C^{r-2} continuity. If the multiplicities of knots are one, B-splines of order r are C^{r-2} continuous. Specifically, B-splines of order four are C^2 continuous with minimised curvature [37].

2) Short support. B-spline basis functions possibly have the shortest support [48]. This results in the estimation of model parameters, predicting and modifying model values can be done locally. The short support also results in band-diagonal observation matrices. The sparse structure can significantly reduce the computational complexity of least-square model estimation to $O(mr^2)$ using QR factorisation, instead of $O(mn^2)$ when using dense matrix inversion [52], where m is the number of sample points.

3) Flexibility. B-splines and NURBS are theoretically flexible to approximate any smooth geometry by choosing sufficient knots. As presented in Figure 2(b-d), B-spline basis functions can be linearly combined to generate different equivalents, such as interpolation (or cardinal), dual and wavelet basis functions. They can be used as a convolution kernel for high-efficiency calculations of interpolation, parameter estimation and multi-resolution analysis (MRA) [48], instead of a general matrix inversion. This is very useful when manipulating large body of data.

4) Optimised time-frequency localising capability. A B-spline interpolant of order four as plotted in Figure 2(b), shows exponentially faster decay than the traditional, band-limited interpolant – sinc [8]. As presented in Figure 1(a), B-spline basis functions converge to Gaussian as the order increases. A B-spline basis of order four has already optimised time-frequency bandwidth product, within the 1% limit specified by the uncertainty principle [53].

5) Simplicity. B-spline basis functions can be easily calculated using de Boors' recursion formula from a square wave function. Derivatives and integrals can also be conveniently calculated from corresponding lower or higher orders of basis functions [37].

6) Affine invariance. B-spline model coefficients are called control points, which are affine invariant to B-splines. If an affine transformation, such as translation, rotation, scaling and shear, is applied to a B-spline, the result can be simply calculated by transforming its control.

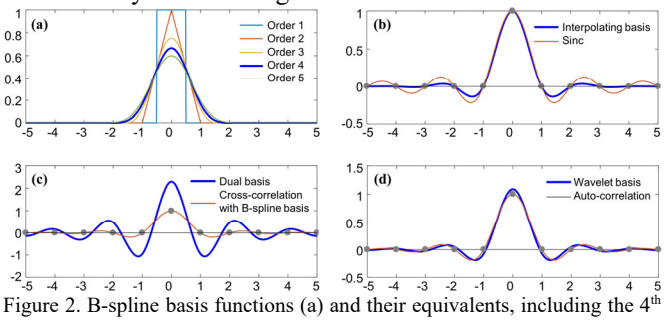

Figure 2. B-spline basis functions (a) and their equivalents, including the 4th order interpolation basis (b), the dual basis (c) and the wavelet basis (d).

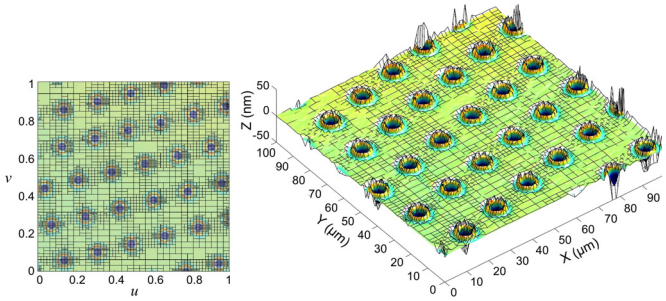

Figure 3. Approximation of the hard-disk landing zone using T-splines. (a) A parametric space view and (b) a physical space view of the T-model, which uses 4900 control points to achieve to a peak to valley error of 1 nm.

B-spline and NURBS surfaces are tensor product models. Tensor product models have regular control point grids, which are suitable for isotropic signal characterisation, e.g. machined surfaces with uniformly distributed tool marks. However, they are not optimal for freeform, structured surfaces. Instead, advanced B-splines using truncated control point nets, i.e. T-splines [28, 54-57], have proved to be optimised in control point mesh management. Figure 3 demonstrates that the previous laser textured surface of Figure 1(d) can be reconstructed to the same error level using a T-spline, with a limited number of control points that is approximately one third of that when using a NURBS.

T-splines breaks the topological limit of tensor-product grids. However, they may lead to increased computational complexity, and the basis functions are not of a partition of unity or linear independence. Therefore, advanced T-splines, e.g. analysis-suitable T-splines [58], are still in development. Thus, geometric approximation and characterisation using T-splines is still at an initial stage.

1.3. The contribution

In this paper, we initially proposed to characterise freeform, structured surfaces in T-spline spaces, using a developed local

fitting algorithm. Similarly to what B-splines do in signal characterisation [37], we demonstrate that the T-spline fitting can be used to cope with most of the aforementioned challenges, including freeform removal, noise removal and filtration, interpolation and reconstruction, smart down-sampling and data compression, with improved performance on computing efficiency.

2. Locally fitted T-splines

2.1. The algorithm

T-splines with a fast local fitting algorithm [34, 59], namely locally fitted T-splines, are introduced. Given a set of control points $\boldsymbol{p}_i \in \mathbb{R}^d$ and an associated 2D mesh of knots Φ with T-junctions, i.e. T-mesh as seen in Figure 4, a T-spline surface is defined as follows:

$$\boldsymbol{f}(s,t) = \frac{\sum_{i=1}^{n} \boldsymbol{p}_i b_i(s,t)}{\sum_{i=1}^{n} b_i(s,t)} = \left[\sum_{i=1}^{n} b_i(s,t)\right]^{-1} \boldsymbol{bP}, \qquad (2)$$

where (s,t) is a parametric location in a domain $\Omega \in \mathbb{R}^2$; b_i is the i^{th} blending function, i.e. basis function, associated to the i^{th} knot vertex, with $\boldsymbol{b}$ being a row vector comprising $b_i(s,t)$; while $\boldsymbol{P}$ is an n-by-d control point matrix. If all the knot junctions of a T-mesh are cross-shaped, it degenerates into a B-spline knot mesh, or B-lattice. The i^{th} blending function has the following tensor product form:

$$b_i(s,t) = \beta_{\boldsymbol{s}_i}(s)\,\beta_{\boldsymbol{t}_i}(t), \qquad (3)$$

with $\beta_{\boldsymbol{s}_i}$ and $\beta_{\boldsymbol{t}_i}$ being respectively the B-spline basis functions supported by local knot vectors $\boldsymbol{s}_i$ and $\boldsymbol{t}_i$, which can be inferred following Sederberg's rule one [28]. Examples of cubic blending functions are presented in Figure 4(a).

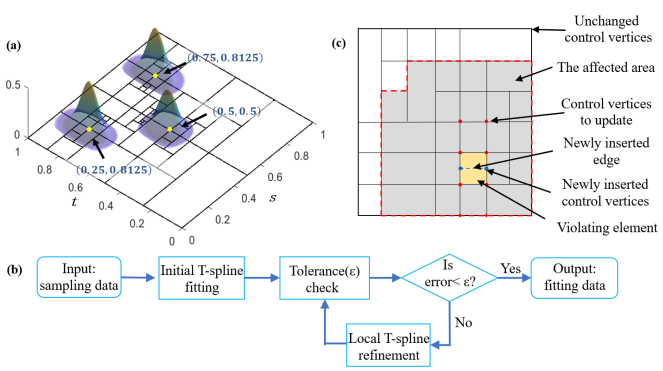

Figure 4. Definition of the locally fitted T-splines. (a) Three blending functions of a T-mesh, (b) the iterative fitting process flow and (c) the local characteristics of the fitting. In the local refinement process, if a T-mesh element (yellow) is split, two new knots or vertices (blue dots) with a connecting edge are introduced. Due to the local support, only the neighbour knots (red dots)-associated blending functions alter. Fitting of the new and neighbour knots-assoxiated control points using the local data in the affected area (gray) instead of global fitting can, thus reduce the computational complexity.

As presented in Figure 4(b), the locally fitted T-splines follows the computational flow of general, locally refined T-splines [60]. In each refining iteration, the violating T-mesh element, which contains the points that have the Euclidean fitting errors larger than a preset threshold ε, is split dyadically. The control point matrix $\boldsymbol{P}$ of the refined T-meshes are then updated by solving the least squares problem as shown below:

$$\min \sum_{j=1}^{m} \left\| \boldsymbol{v}_j - \boldsymbol{f}(s_j,t_j) \right\|^2 = \min \left\| \boldsymbol{V} - \operatorname{diag}\left(\sum_{i=1}^{n} b_{i,j} \right) \boldsymbol{BP} \right\|^2, \qquad (4)$$

where $\boldsymbol{V}$ is an m-by-d measurement matrix comprised of the sampling points $\boldsymbol{v}_j$, and $\boldsymbol{B}$ is an m-by-n model matrix with the j^{th} row, i^{th} column element $b_{i,j} = b_i(s_j,t_j)$. The corresponding parametric location (s_j,t_j) of each sampling point can be obtained using conformal mapping algorithms [61] or using normalised x and y coordinates [60].

To ensure the computational efficiency, Eq.(4) is solved using a local fitting strategy instead of a global fitting. As presented in Figure 4(c), for each refined element, only the neighbour control points $\boldsymbol{P}_L$ with altered blending functions are updated, using the sampling data in a local, affected area. This local fitting can be expressed by solving the following equation:

$$\operatorname{diag}\left(\sum_{i=1}^{n} b_{i,j} \right) \boldsymbol{V}_K = \boldsymbol{B}_{K\times N}\boldsymbol{P}_N = \boldsymbol{B}_{K\times L}\boldsymbol{P}_L + \boldsymbol{B}_{K\times(N-L)}\boldsymbol{P}_{N-L}, \qquad (5)$$

where K denotes the sampling point indices of an affected area; N denotes all the control point indices of a T-spline; L and (N-L) denote respectively the index sets of the updated and the remaining control points. Thus, the updated control points can be efficiently calculated using

$$\boldsymbol{P}_L = \boldsymbol{B}_{K\times L}^{+}\left[\operatorname{diag}\left(\sum_{i=1}^{n} b_{i,j} \right) \boldsymbol{V}_K - \boldsymbol{B}_{K\times(N-L)}\boldsymbol{P}_{N-L} \right], \qquad (6)$$

where $\cdot^{+}$ denotes a matrix pseudo-inverse. Because $\boldsymbol{B}_{K\times(N-L)}$ and $\boldsymbol{P}_{(N-L)}$ can inherit from the previous iteration, calculation of Eq.(6) degenerates into a small-scale least squares problem, which is solved using the pseudo-inverse of $\boldsymbol{B}_{K\times L}$. In other words, the local fitting speeds up the computation significantly by reducing the matrix dimension of pseudo-inverse from $m \times n$ to $|K| \times |L|$, where $|\cdot|$ denotes the size of a set.

2.2. Performance evaluation

The locally fitted T-spline algorithm was evaluated by comparing it with simple global fitting [60] regarding fitting accuracy and computational time costs. Two typical z-map data were used as experimental objects. One is the hard-disk surface previously used with sparse, repetitive bumps. Another one is a steel plate topography with randomly distributed particles. The analysing results are presented in Figure 5, where the fitting accuracy is indicated using the signal-to-noise ratio (SNR), i.e.

$$SNR = 10\lg\left[\frac{\sum_{j=1}^{m}\left\|\boldsymbol{v}_j\right\|^2}{\sum_{j=1}^{m}\left\|\boldsymbol{f}(s_j,t_j)-\boldsymbol{v}_j\right\|^2}\right]. \quad (7)$$

The SNR normalises the reconstruction errors so that the results of different surface samples are comparable.

The results show that the locally fitted T-splines can approximate the complex surface topographies with reasonably small fitting errors. The computational time costs are about 1/4~1/2 of that of the global fitting-based T-splines. The higher the fitting SNR, the more significant the decrease in computational time.

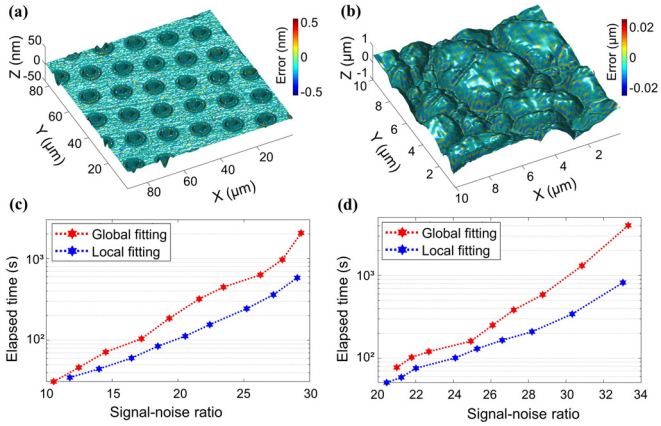

Figure 5. Performance evaluation of the locally fitted T-splines. Typical fitting results of a hard-disk surface (a) and steel plate surface (b) with pseudo-coloured fitting errors, and their corresponding computational time cost analysis versus different root mean squared fitting errors (c-d), compared to that with general global fitting-based T-splines.

3. Freeform removal

Arbitrary freeform surface topography can be described in the following parametric form [21]:

$$(x,y,z)^T = \boldsymbol{q}(s,t) = \boldsymbol{q}_{\text{form}}(s,t) + q_{\text{res}} \cdot \boldsymbol{n}(s,t) \quad (8)$$

where $\boldsymbol{q}$ is a 3D surface point defined on a 2D parametric location (s,t); $\boldsymbol{q}_{\text{form}}$ and q_{res} are respectively an underlying form and residual S-F surface topography, i.e. surface texture [1]; $\boldsymbol{n}$ is the local norm vector of the form. Once a form is fitted, surface texture can be extracted as a simple height map for post-analysis, such as filtration and pattern recognition.

To demonstrate the freeform removal performance of T-spline fitting, we conducted the first case study using simulations. As presented in Figure 6(a-c), a saddle-shaped surface with superimposed surface texture was first generated. Using an initial, empty T-mesh, i.e. a B-lattice without splits expect border extensions [29], and setting the maximum fitting error threshold as 0.5, an ordinary fit of the data using the above iterative algorithm was implemented. In this case, x- and y-data are normalised as the parameters, while z-data are fitted by scalar control points. The ordinary fit result shows enlarged magnitudes of surface texture in the area of high slopes. Using the same initial T-mesh and algorithm, an orthogonal distance fit was also implemented. In this case, the point cloud was conformally mapped [61] to parameter points in a square domain of $\mathbb{R}^2$, with which sample points were fitted by 3D control points. The results show that the extracted surface texture coincided well with the simulated one, without obvious distortion. It must be noted that the final resulted splines are simple B-splines in the simulation, due to the simplicity of the surface.

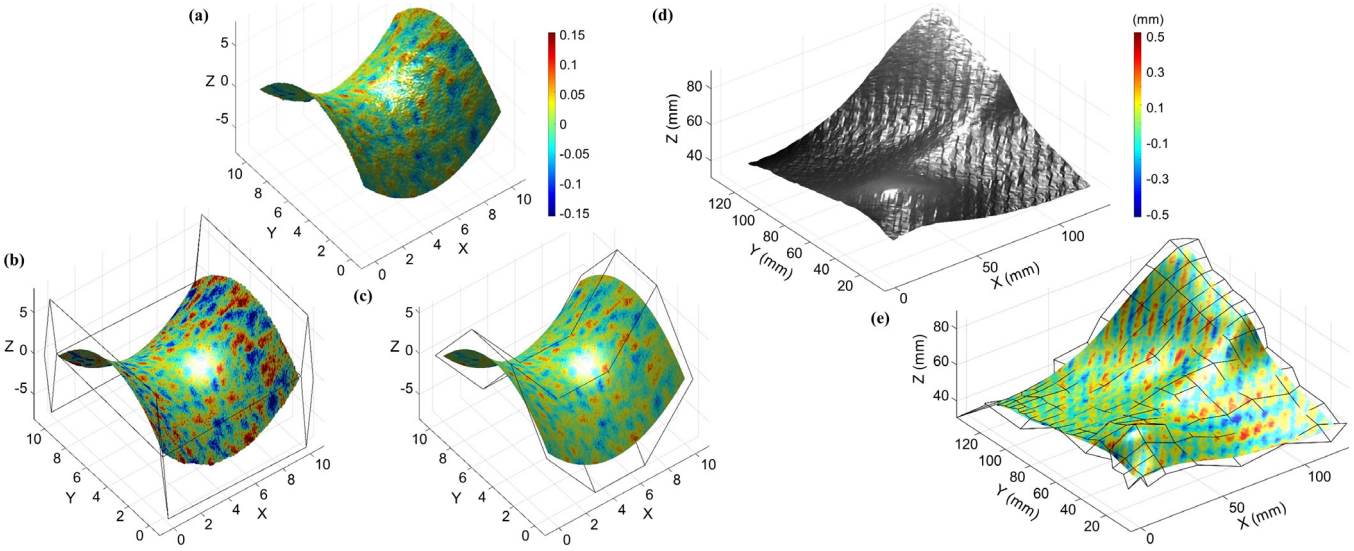

Figure 6. Freeform removal from a simulated saddle surface and a real artefact. (a) The simulated saddle surface with additive artificial, surface texture (pseudo-coloured) of Gaussian process with an *Sq* of 0.033; (b) an ordinary T-spline fitting results in a remaining surface texture with an *Sq* of 0.062; (c) a parametric space T-spline fitting results in a remaining surface texture with an *Sq* of 0.032. (d) The freeform artefact with visible tool marks measured using a structured light scanner and (e) a parametric space T-spline form-fitting results in a remaining surface texture with an *Sq* of 0.139 mm.

T-spline fitting was then applied to an artificial freeform artefact measured using a structured light scanner [62]. As presented in Figure 6(d), the freeform surface shows visible tool marks, which are the main components of surface texture to be extracted. By using conformally mapped parameters as the independent variables and setting the maximum fitting error threshold as 0.8 mm, the 3D sample points were fitted, using the iterative algorithm. The result in Figure 6(e) shows that the tool marks were properly extracted with an *Sq* of 0.139 mm.

4. Shape-preserving filtration with MRA

The T-spline fitting can be applied for geometric filtration with notable shape-preserving capabilities. If a Euclidean fitting error threshold is used as the filtering index, filtered results of a measured step surface are initially presented in Figure 7. The figures show that the filtered surface contains smaller scales of components when the index diminishes gradually. The results show significant edge-preserving performance, as the remaining texture shows uniform irregularities across the surface including the regions of edges.

However, the above fitting error-indexed T-spline filtration lacks accurate cut-off control of frequency or scales. To address the issue, we first consider the filtration problem in nested B-spline spaces [63, 64]. We follow the convention of [63] to define a hierarchy of B-lattices $\{\Phi^{n\in\mathbb{Z}}\}$ overlaid on a parametric domain $\Omega \in \mathbb{R}^2$, e.g. $[0,1] \times [0,1]$, each of which has a total of $(n+3) \times (n+3)$ uniformly distributed knots of spacing $1/(n+1)$, with indices from -1 to $(n+1)$ on both parametric dimensions. Let V^n be a space of uniform B-spline functions defined on Φ^n, then any function of Φ^n with $(n+3) \times (n+3)$ control points, can be exactly represented by a function of Φ^{n+1} with $(2n+3) \times (2n+3)$ control points, using B-spline refinement or knot insertion algorithms [51, 63]. Thus, the increasingly resolution-refined B-splines nested relationship is guaranteed:

$$V^0 \subset V^1 \subset \cdots \subset V^n \subset \cdots. \tag{9}$$

The locally fitted T-splines degenerate to the above hierarchical B-splines, providing the fitting error threshold of refinement $\varepsilon \to 0$. In general cases with $\varepsilon > 0$, the nesting relationship holds if only the refining topology is followed, as described in [28]. For the dyadic split topology used in the locally fitted T-splines, the nesting relationship in Eq. (8) can only be held approximately. However, we benefitted from their simplicity at the initial stage. Figure 8 presents a multi-resolution analysis of an artificial, freeform surface data, using the above iterative algorithm with a slight modification, where local fitting calculations are applied to the residual maps from a global approximation and previous iterations. The results show visibly fitting resolution improvement and a remarkable approximation to the original surface.

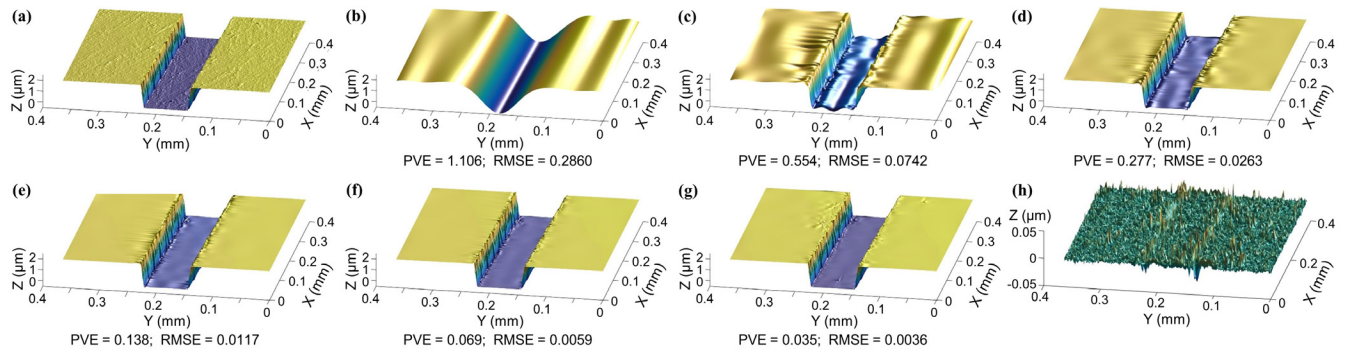

Figure 7. Edge-preserving filtering of a step surface. (a) The original surface, (b-g) filtered results using the maximum fitting error thresholds of 1/2, 1/4, 1/8, 1/16, 1/32 and 1/64 respectively of the surface magnitude, (h) remaining surface roughness subtracted from (g).

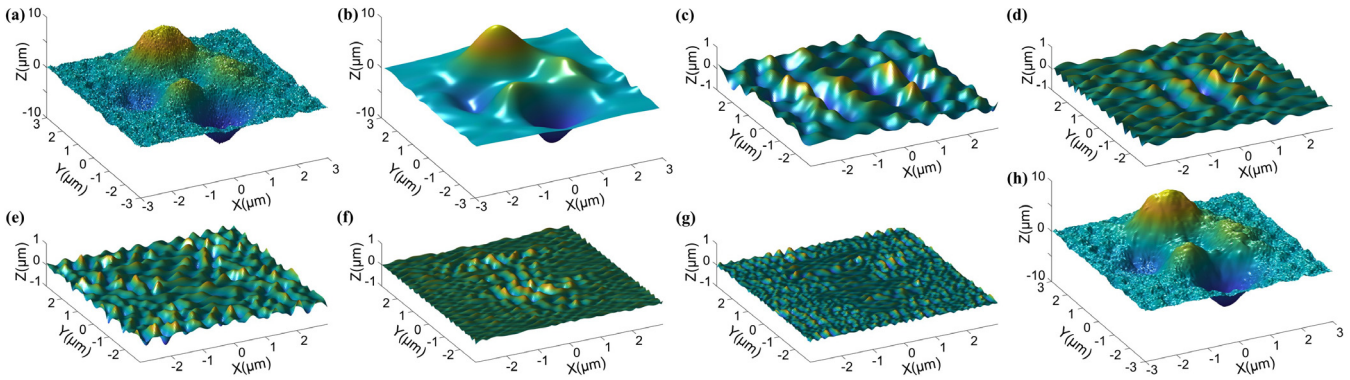

Figure 8. Multi-resolution analysis of the Matlab Peaks function with additive Gaussian process noise. (a) The original surface, (b) an initial approximation of the original surface using a B-lattice, (c-g) locally fitted T-spline approximations of the residual maps using iteratively refined T-meshes, (h) synthesised surfaces using the data of (b-g).

5. Missing data Interpolation

Missing data are widely found in surface topography measurement. Figure 9(a) shows a typical surface topography with missing data obtained using a focus variation microscope. The majority of existing topography processing algorithms, e.g. filtration, the Fourier transform and auto-correlation, only work for grid data. This indicates that missed data need to be filled.

The selected surface sample is a structured surface with missing data at both the feature edges and centres, with a high missing rate of 21.1%. Figure 9(b-c) report an interpolation result of the structured surface using the locally fitted T-spline fitting. For reference, an interpolation result using multi-level B-splines (probably the most stable interpolation method up to now) [63] with an equivalent level is presented in Figure 9(b). The result illustrates that locally fitted T-splines performs equivalently as multi-level B-splines, but with an adaptive knot mesh.

However, it needs to be noted that the T-spline interpolation result has slightly visible ripples at the feature edges. Besides, the experiment was not an exact interpolation due to the smoothing effect. Exact interpolation using T-splines was abandoned for this case, because it was found to consume an unacceptable time cost, with extremely dense T-meshes. Interpolation algorithms with T-splines need to be improved.

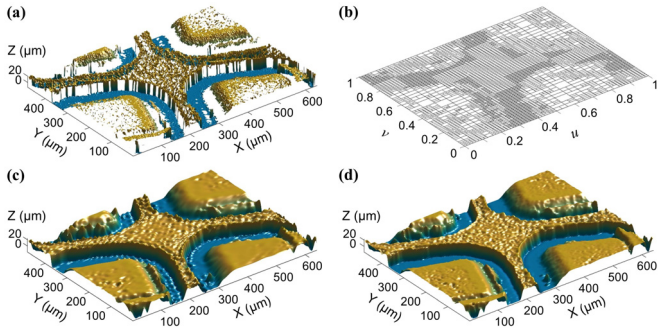

Figure 9. Missing data interpolation for a structured surface. (a) Raw data from a focus variation microscope, (b-c) a locally fitted T-mesh and its interpolation result, (d) interpolation using an equivalent eight-level B-splines with a minimum knot spacing of 0.004 in the parametric space,.

6. Smart down-sampling and data compression

6.1. Smart down-sampling

Optical, areal surface topography measurement usually produce sizable measurement data, particularly in on-line metrology. Smart down-sampling of the large measurement data with limited or without accuracy loss, is highly expected for storage space-saving; thus, reducing the cost of production management. Based on the shift-invariant spacing sampling theory [49], we have shown in [34] that an arbitrary surface in a T-spline space can be exactly recovered from several smartly designed sample points, based on least squares regression. Here, we apply the smart sampling method, namely T-patch sampling [34], to execute data down-sampling.

Firstly, the locally refined T-spline algorithm is applied which maps an arbitrary surface to an approximated T-spline space. The T-patch sampling is then applied, which randomly or uniformly selects from each T-mesh element with several data points. Theoretically, four sample points within an element are enough to recover the surface without accuracy loss, in a spline space. In the surface recovery stage, the down-sampled data are used to estimate the control points of the T-spline, using least squares regression. Thus the original surface can be recovered at any observing location. A down-sampling case study is presented in Figure 10. A 9300 control points T-spline metamodel with an RMSE of 0.1 nm was fitted to the original surface. Subsequently, the T-patch sampling, with different sample sizes, was implemented and the reconstruction accuracy was analysed. Compared with popular, existing sampling strategies, the T-patch sampling indicates up to half an order of magnitude reduction of reconstruction error or sample size, for the same level of sample size or sampling accuracy requirement. More case studies can be found in [34].

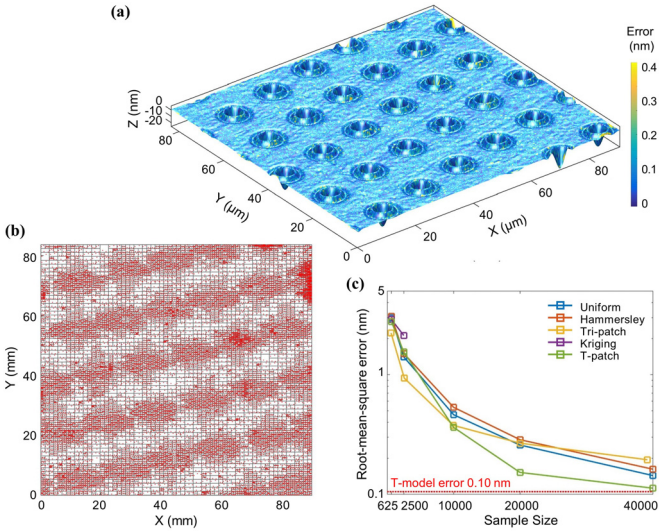

Figure 10. Accuracy analysis of smart-down sampling in T-spline spaces. (a) Reconstructed hard-disk surface topography with pseudo-coloured errors from a T-patch sample set of 20,000 points, based on a T-spline model with 9300 control points in (b); (c) a statistic of the sampling errors by applying different sampling strategies to the structured surface.

6.2. Data compression

Conversion of a point cloud to T-splines can be used for data compression, by saving a corresponding T-spline model instead of the point set itself. A T-spline surface is completely determined by its control mesh, including the 2D coordinates of its control vertices or knots, the corresponding topological

connections of each vertex, and the corresponding control point coordinates. With a T-spline model, surface topography with an arbitrary resolution can be recovered.

Considering that surface topography data are usually in the form of z-maps, we assume that a control point is saved in double using 8 bytes; a 2D control vertex or knot is saved in single using 8 bytes; four corresponding connection indices are saved in short using 8 bytes. This indicates that, a total number of 24 bytes are required for saving a control point. Compared to *z*-maps which use 8 bytes to save a sample point, a T-spline model can achieve compression only if the number of control points is, at most, one third that of sampling points. For the majority of freeform, structured surfaces which can be efficiently characterised using T-splines, data compression with reduced sizes of storage can usually be achieved. Figure 11 presents a compression rate analysis of two complex surface topographies. The results reveal that the compression was achieved with reasonably small approximation errors.

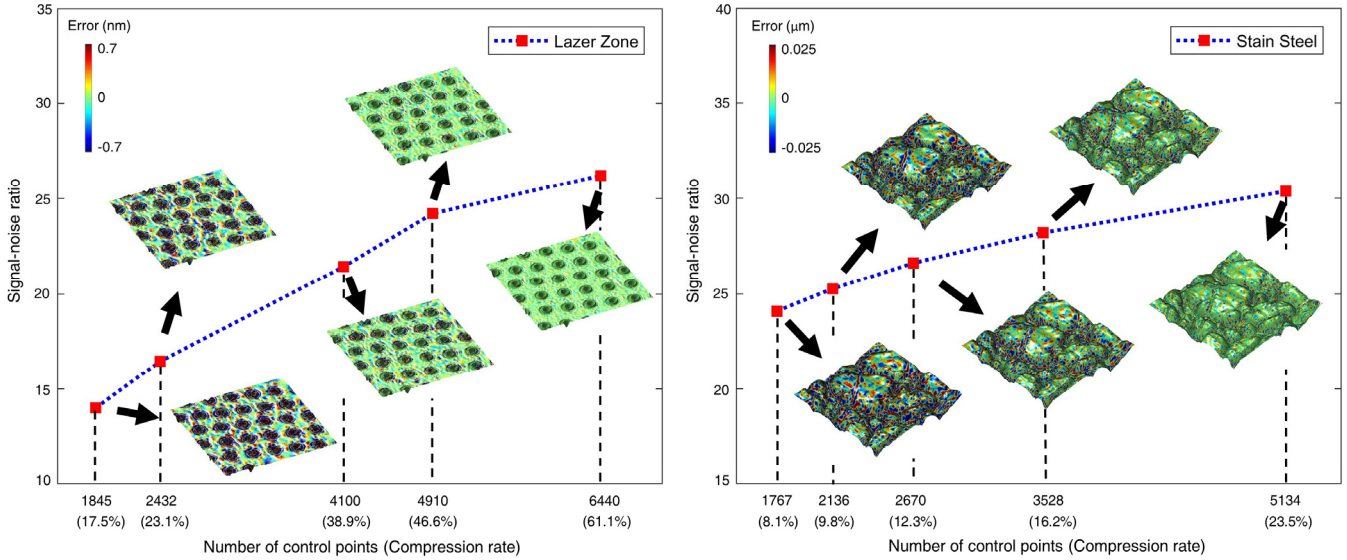

Figure 11. Compression rate analysis using the locally fitted-splines for periodically laser-textured bumps (a) and steel plate with random particles (b).

7. Conclusion

In this paper, a locally fitted T-spline fitting method is proposed for the characterisation of freeform, structured surfaces. Several case studies were provided, including freeform removal in non-Euclidean spaces, filtration with shape-preserving capabilities and multi-resolution analysis, missing data interpolation, smart down-sampling and data compression. Similar to B-splines, T-splines should also work for surface matching and stitching, feature extraction, contouring and geometrical morphing, though they are not presented at the initial stage of development.

However, the proposed method is not perfect at the moment. We have found that, the iterative results do not always have a monotonous convergence. This could be because in each iteration, only the local control points with altered blending functions are updated, which cannot adapt to the situations with complex local behaviours. Second, the least squares-based model estimation may produce ripples when fitting complex geometries, e.g. interpolation, using a very dense T-mesh, particularly those with significant noise. Third, the algorithm complexity increases, though T-splines show useful control point saving in comparison with B-splines. The computational efficiency of the algorithm still needs to be optimised.

Acknowledgements

This project is supported by the National Natural Science Foundation of China (Grant No. 52075206, 51835005 and 51705178).

References

[1] R. Leach, *Fundamental Principles of Engineering Nanometrology*. Elsevier Science, 2014.
[2] R. Leach *et al.*, *Characterisation of areal surface texture*. Springer, Berlin, 2013.
[3] ISO 4287, "Geometrical Product Specifications (GPS) — Surface texture: Profile method — Terms, definitions and surface texture parameters," 1997, International Organization of Standardization, Geneva.
[4] ASME B46.1, "Surface Texture (Surface Roughness, Waviness, and Lay)", 2019, ASME.
[5] ISO 25178-2, "Geometrical product specification (GPS) - Surface texture: areal - part 2: terms, definitions and surface texture parameters," 2012, International Organization of Standardization, Geneva.
[6] ISO 16610-1, "Geometrical product specifications (GPS) -- Filtration -- Part 1: Overview and basic concepts," 2015, International Organization of Standardization, Geneva.

[7] C. A. Brown *et al.*, "Multiscale analyses and characterizations of surface topographies," *CIRP Annals,* vol. 67, no. 2, pp. 839-862, 2018, doi: 10.1016/j.cirp.2018.06.001.
[8] T. D. B. Jacobs, T. Junge, and L. Pastewka, "Quantitative characterization of surface topography using spectral analysis," Surface Topography: Metrology and Properties, vol. 5, no. 1, p. 013001, 2017, doi: 10.1088/2051-672x/aa51f8.
[9] P. J. Scott, "Feature parameters," *Wear,* vol. 266, no. 5-6, pp. 548-551, 2009.
[10] S. Lou, L. Pagani, W. Zeng, X. Jiang, and P. J. Scott, "Watershed segmentation of topographical features on freeform surfaces and its application to additively manufactured surfaces," *precision engineering,* vol. 63, pp. 177-186, 2020, doi: 10.1016/J.PRECISIONENG.2020.02.005.
[11] X. Jiang and P. Scott, *Advanced metrology - Freeform surfaces*. Huddersfield, UK: Academic Press, 2020, p. 374.
[12] X. J. Jiang and D. J. Whitehouse, "Technological shifts in surface metrology," *CIRP Annals - Manufacturing Technology,* vol. 61, no. 2, pp. 815-836, 2012, doi: 10.1016/j.cirp.2012.05.009.
[13] A. A. G. Bruzzone, H. L. Costa, P. M. Lonardo, and D. A. Lucca, "Advances in engineered surfaces for functional performance," *CIRP Annals - Manufacturing Technology,* vol. 57, no. 2, pp. 750-769, 2008.
[14] D. Gropper, L. Wang, and T. J. Harvey, "Hydrodynamic lubrication of textured surfaces: A review of modeling techniques and key findings," *Tribology International,* vol. 94, pp. 509-529, 2016, doi: 10.1016/j.triboint.2015.10.009.
[15] C. Gachot, A. Rosenkranz, S. M. Hsu, and H. L. Costa, "A critical assessment of surface texturing for friction and wear improvement," *Wear,* vol. 372-373, pp. 21-41, 2017, doi: 10.1016/j.wear.2016.11.020.
[16] A. Malshe, K. Rajurkar, A. Samant, H. N. Hansen, S. Bapat, and W. Jiang, "Bio-inspired functional surfaces for advanced applications," *CIRP Annals - Manufacturing Technology,* vol. 62, no. 2, pp. 607-628, 2013, doi: 10.1016/j.cirp.2013.05.008.
[17] H. Lee *et al.*, "Transferable ultra-thin multi-level micro-optics patterned by tunable photoreduction and photoablation for hybrid optics," *carbon,* vol. 149, pp. 572-581, 2019, doi: 10.1016/J.CARBON.2019.04.085.
[18] L. Müller-Meskamp *et al.*, "Efficiency enhancement of organic solar cells by fabricating periodic surface textures using direct laser interference patterning," *Advanced Materials,* vol. 24, no. 7, pp. 906-910, 2012, doi: 10.1002/adma.201104331.
[19] X. Jiang, P. Cooper, and P. J. Scott, "Freeform surface filtering using the diffusion equation," *Proceedings of the Royal Society A: Mathematical physical and engineering sciences,* vol. 467, no. 2127, pp. 841-859, 2011, doi: 10.1098/RSPA.2010.0307.
[20] H. S. Abdul-Rahman, S. Lou, W. Zeng, X. Jiang, and P. J. Scott, "Freeform texture representation and characterisation based on triangular mesh projection techniques," *measurement,* vol. 92, pp. 172-182, 2016, doi: 10.1016/J.MEASUREMENT.2016.06.005.
[21] L. Pagani *et al.*, "Towards a new definition of areal surface texture parameters on freeform surface: Re-entrant features and functional parameters," *Measurement,* vol. 141, pp. 442-459, 2019, doi: 10.1016/j.measurement.2019.04.027.
[22] S. Lou, S. S. Brown, W. Sun, W. Zeng, X. Jiang, and P. Scott, "An investigation of the mechanical filtering effect of tactile CMM in the measurement of additively manufactured parts," *measurement,* vol. 144, pp. 173-182, 2019, doi: 10.1016/J.MEASUREMENT.2019.04.066.
[23] H. S. Abdul-Rahman, X. J. Jiang, and P. J. Scott, "Freeform surface filtering using the lifting wavelet transform," *Precision Engineering,* vol. 37, no. 1, pp. 187-202, 2013, doi: 10.1016/j.precisioneng.2012.08.002.
[24] M. Wang, Y.-P. Shao, S.-C. Du, and L.-f. Xi, "A diffusion filter for discontinuous surface measured by high definition metrology," *International Journal of Precision Engineering and Manufacturing,* vol. 16, no. 10, pp. 2057-2062, 2015, doi: 10.1007/s12541-015-0267-y.
[25] G. Guennebaud and M. Gross, "Algebraic point set surfaces," *ACM Trans. Graph.,* vol. 26, no. 3, p. 23, 2007, doi: 10.1145/1276377.1276406.
[26] I. Raid, T. Kusnezowa, and J. Seewig, "Application of ordinary kriging for interpolation of micro-structured technical surfaces," *Measurement Science and Technology,* vol. 24, no. 9, p. 095201, 2013.
[27] A. Gálvez and A. Iglesias, "Particle swarm optimization for non-uniform rational B-spline surface reconstruction from clouds of 3D data points," *Information Sciences,* vol. 192, pp. 174-192, 2012, doi: 10.1016/j.ins.2010.11.007.
[28] T. W. Sederberg, D. L. Cardon, G. T. Finnigan, N. S. North, J. Zheng, and T. Lyche, "T-spline simplification and local refinement," *ACM Transactions on Graphics,* vol. 23, no. 3, p. 276, 2004.
[29] J. Wang, Y. Lu, L. Ye, R. Chen, and R. Leach, "Efficient analysis-suitable T-spline fitting for freeform surface reconstruction and intelligent sampling," *Precision Engineering,* vol. 66, pp. 417-428, 2020, doi: 10.1016/j.precisioneng.2020.08.008.
[30] F. E. Talke, "Surface texture for magnetic recording," in *Encyclopedia of Tribology*, Q. J. Wang and Y.-W. Chung eds. Boston, MA: Springer US, 2013, pp. 3485-3489.
[31] B. M. Colosimo, Q. Semeraro, and M. Pacella, "Statistical process control for geometric specifications: On the monitoring of roundness profiles," *Journal of Quality Technology,* vol. 40, no. 1, pp. 1-18, 2008, doi: 10.1080/00224065.2008.11917709.
[32] M. Colledani *et al.*, "Design and management of manufacturing systems for production quality," *CIRP Annals - Manufacturing Technology,* vol. 63, no. 2, pp. 773-796, 2014.
[33] A. Weckenmann *et al.*, "Multisensor data fusion in dimensional metrology," *CIRP Annals - Manufacturing Technology,* vol. 58, no. 2, pp. 701-721, 2009, doi: 10.1016/j.cirp.2009.09.008.
[34] J. Wang, R. Leach, R. Chen, J. Xu, and X. J. Jiang, "Distortion-free intelligent sampling of sparse surfaces via locally refined T-spline metamodelling," *International Journal of Precision Engineering and Manufacturing-Green Technology,* pp. 1-16, 2020.
[35] J. Wang, X. Jiang, L. A. Blunt, R. K. Leach, and P. J. Scott, "Intelligent sampling for the measurement of structured surfaces," *Measurement Science and Technology,* vol. 23, no. 8, p. 085006, 2012.
[36] Y. Guo, M. Bennamoun, F. Sohel, M. Lu, J. Wan, and N. M. Kwok, "A comprehensive performance evaluation of 3d local feature descriptors," *International Journal of Computer Vision,* vol. 116, no. 1, pp. 66-89, 2016, doi: 10.1007/s11263-015-0824-y.
[37] M. Unser, "Splines: A perfect fit for signal and image processing," *IEEE Signal Processing Magazine,* vol. 16, no. 6, pp. 22-38, 1999, doi: 10.1109/79.799930.

[38] G. Zheng, M. A. Ballester, M. Styner, and L. P. Nolte, "Reconstruction of patient-specific 3D bone surface from 2D calibrated fluoroscopic images and point distribution model,", *Med Image Comput Comput Assist Interv,* vol. 9, no. Pt 1, pp. 25-32, 2006, doi: 10.1007/11866565_4.
[39] S. E. Fick and R. J. Hijmans, "WorldClim 2: new 1-km spatial resolution climate surfaces for global land areas," *International Journal of Climatology,* vol. 37, no. 12, pp. 4302-4315, 2017, doi: 10.1002/joc.5086.
[40] J. Raja, B. Muralikrishnan, and S. Fu, "Recent advances in separation of roughness, waviness and form," *Precision Engineering,* vol. 26, no. 2, pp. 222-235, 2002, doi: 10.1016/S0141-6359(02)00103-4.
[41] ISO 16610-2, "Geometrical product specifications (GPS) — Filtration — Part 22: Linear profile filters: Spline filters," 2015, *International Organization of Standardization, Geneva*.
[42] C. D. Giovampaola, G. Carluccio, F. Puggelli, A. Toccafondi, and M. Albani, "Efficient algorithm for the evaluation of the physical optics scattering by NURBS surfaces with relatively general boundary condition," *IEEE Transactions on Antennas and Propagation,* vol. 61, no. 8, pp. 4194-4203, 2013, doi: 10.1109/TAP.2013.2261447.
[43] H. Pottmann *et al.*, "Freeform surfaces from single curved panels," *ACM Trans. Graph.,* vol. 27, no. 3, pp. 1–10, 2008, doi: 10.1145/1360612.1360675.
[44] A. A. Amini, Y. Chen, M. Elayyadi, and P. Radeva, "Tag surface reconstruction and tracking of myocardial beads from SPAMM-MRI with parametric B-spline surfaces,", *IEEE transactions on medical imaging,* vol. 20, no. 2, pp. 94-103, 2001, doi: 10.1109/42.913176.
[45] Y. Chen, J. Gao, H. Deng, D. Zheng, X. Chen, and R. Kelly, "Spatial statistical analysis and compensation of machining errors for complex surfaces," *Precision Engineering,* vol. 37, no. 1, pp. 203-212, 2013, doi: 10.1016/j.precisioneng.2012.08.003.
[46] D.-J. Yoo, "Three-dimensional surface reconstruction of human bone using a B-spline based interpolation approach," *Computer-Aided Design,* vol. 43, no. 8, pp. 934-947, 2011, doi: 10.1016/j.cad.2011.03.002.
[47] S. Mallat, *A wavelet tour of signal processing: The sparse way*. Elsevier Science, 2008.
[48] M. Unser, "Sampling-50 years after Shannon," *Proceedings of the IEEE,* vol. 88, no. 4, pp. 569-587, 2000, doi: 10.1109/5.843002.
[49] A. Aldroubi and K. Gröchenig "Nonuniform sampling and reconstruction in shift-invariant spaces," *SIAM Rev.,* vol. 43, no. 4, pp. 585-620, 2001, doi: 10.1137/s0036144501386986.
[50] L. A. Piegl and W. Tiller, *The NURBS book*. Springer, 1997, p. 646.
[51] C. de Boor, *A practical guide to splines* (Applied Mathematical Sciences 27). Springer, 2001.
[52] R. M. Barker, M. G. Cox, A. B. Forbes, and P. M. Harris, "Best practice guide no. 4 software support for metrology: Discrete modelling and experimental data analysis," in "Technical report, National Physical Laboratory," Teddington, UK, 2004.
[53] M. Unser, A. Aldroubi, and M. Eden, "On the asymptotic convergence of B-spline wavelets to Gabor functions," *IEEE Transactions on Information Theory,* vol. 38, no. 2, pp. 864-872, 1992, doi: 10.1109/18.119742.
[54] Y. Wang and J. Zheng, "Curvature-guided adaptive T-spline surface fitting," *Computer-aided Design,* vol. 45, no. 8, pp. 1095-1107, 2013.
[55] J. Deng *et al.*, "Polynomial splines over hierarchical T-meshes," *Graphical Models,* vol. 70, no. 4, pp. 76-86, 2008, doi: 10.1016/j.gmod.2008.03.001.
[56] T. Dokken, T. Lyche, and K. F. Pettersen, "Polynomial splines over locally refined box-partitions," *Computer Aided Geometric Design,* vol. 30, no. 3, pp. 331-356, 2013, doi: 10.1016/j.cagd.2012.12.005.
[57] C. Feng and Y. Taguchi, "FasTFit: A fast T-spline fitting algorithm," *Computer-Aided Design,* vol. 92, pp. 11-21, 2017, doi: 10.1016/j.cad.2017.07.002.
[58] X. Li and M. A. Scott, "Analysis-suitable T-splines: Characterization, refineability, and approximation," *Mathematical Models and Methods in Applied Sciences,* vol. 24, no. 06, pp. 1141-1164, 2013, doi: 10.1142/S0218202513500796.
[59] J. Wang, Y. Lu, L. Ye, R. Chen, and R. Leach, "Efficient analysis-suitable T-spline fitting for freeform surface reconstruction and intelligent sampling," *Precision Engineering,* vol. 66, pp. 417-428, 2020.
[60] J. Zheng, Y. Wang, and H. S. Seah, "Adaptive T-spline surface fitting to z-map models," in *international conference on computer graphics and interactive techniques*, 2005, pp. 405-411.
[61] T. Meng, G. Choi, and L. Lui, "TEMPO: Feature-endowed teichmüller extremal mappings of point clouds," *SIAM Journal on Imaging Sciences,* vol. 9, no. 4, pp. 1922-1962, 2016, doi: 10.1137/15M1049117.
[62] J. Wang, L. Pagani, R. K. Leach, W. Zeng, B. M. Colosimo, and L. Zhou, "Study of weighted fusion methods for the measurement of surface geometry," *Precision Engineering,* vol. 47, pp. 111-121, 2016, doi: 10.1016/j.precisioneng.2016.07.012.
[63] L. Seungyong, G. Wolberg, and S. Sung-Yong, "Scattered data interpolation with multilevel B-splines," *Visualization and Computer Graphics, IEEE Transactions on,* vol. 3, no. 3, pp. 228-244, 1997, doi: 10.1109/2945.620490.
[64] C. Giannelli, B. Jüttler, and H. Speleers, "THB-splines: The truncated basis for hierarchical splines," *Computer Aided Geometric Design,* vol. 29, no. 7, pp. 485-498, 2012, doi: 10.1016/j.cagd.2012.03.025.